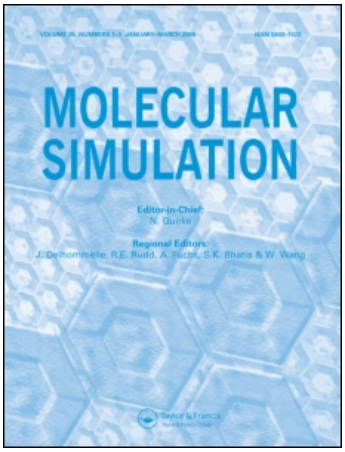

Molecular Simulation
Publication details, including instructions for authors and subscription information:
http://www.informaworld.com/smpp/title~content=t713644482

Multiscale simulation of flow-induced texture formation in polymer liquid crystals and carbonaceous mesophases

D. Grecov[a]; L.R.P. De Andrade Lima[a]; A. D. Rey[a]
[a] Department of Chemical Engineering, McGill University, Montreal, QC, Canada

To cite this Article Grecov, D. , Lima, L.R.P. De Andrade and Rey, A. D.(2005) 'Multiscale simulation of flow-induced texture formation in polymer liquid crystals and carbonaceous mesophases', Molecular Simulation, 31: 2, 185 — 199
To link to this Article: DOI: 10.1080/08927020412331332604
URL: http://dx.doi.org/10.1080/08927020412331332604

Molecular Simulation, Vol. 31, No. 2–3, 15 February–15 March 2005, 185–199

Multiscale simulation of flow-induced texture formation in polymer liquid crystals and carbonaceous mesophases

D. GRECOV, L.R.P. DE ANDRADE LIMA and A.D. REY*

Department of Chemical Engineering, McGill University, 3610 University Street, Montreal, QC, Canada H3A 2B2

(Received April 2004; in final form November 2004)

This paper presents theory and simulation of flow-induced structures in liquid crystalline materials, useful to the creation of synthetic material structures and to the biomimetics of natural fibers. A multiscale theory and simulation of hydrodynamic texture formation is presented; it provides fundamental principles for control and optimization of structures in liquid crystal polymers and carbonaceous mesophases. In thermotropic flow-aligning nematic polymers it is found that as the shear-rate increases, the pathway between an oriented non-planar state and an oriented planar state is through meso-texture formation and coarsening, with temperature and shear rate being efficient fields to control the grain size of the texture. For capillary flow of carbonaceous mesophases, the simulations predict the emergence of macroscopic ring patterns whose thickness and density can be controlled by the applied pressure drops. The results provide insight on microstructure formation and control in liquid crystalline materials.

Keywords: Liquid crystal polymers; Carbonaceous mesophases; Shear flow; Capillary flow; Texture; Disclinations

1. Introduction

The orientational order of liquid crystals offers a unique pathway to create new nano- and microstructures with unique optical, electromagnetic, and mechanical properties. In addition, liquid crystal biomimetics offers the appropriate tools to understand how nature produces high performance fibers, such as spider silk. This paper presents theory and simulation of flow-induced structures (macro-textures and meso-textures), useful to the creation of synthetic material structures and to biomimetics of natural fibers.

Liquid crystals are viscoelastic materials and their remarkable rheological properties are governed by the flow-induced evolution of molecular configurations. Furthermore, the frozen-in microstructure that develops in processing flows dictates the physical properties of the final product. Liquid crystal precursors used in the manufacturing of fibers and films include thermotropic rod-like nematic liquid crystal polymers (LCPs) and low-molecular weight carbonaceous discotic nematic mesophases (CMs). The manufacturing of fibers and films based on liquid crystalline precursors usually involves complex processing flows, and hence good rheological models are needed for product optimization and control. As indicated above, these two materials (LCP and CM) differ in the molecular shape and in their molecular weights. The main impact of molecular weight on rheology is embodied in the Deborah number (De), or ratio of molecular time scale to flow time scale. For low-molecular weight carbonaceous mesophases the De is less than one and hence molecular elasticity can be neglected, and only the orientation process is relevant; for this material the simulations are performed using the Leslie–Ericksen model, described below. The partial orientational order of the molecular unit vector **u** is along the average orientation given by the director vector $\mathbf{n}$ ($\mathbf{n}\cdot\mathbf{n} = 1$) (see figure 1(a)). In contrast, for liquid crystal polymers under sufficiently high shear rates, the De can be arbitrary, and hence molecular elasticity must be retained in addition to the orientation process. For this material the simulations are performed using the Landau–de Gennes model, described below.

Nematic liquid crystals (NLCs) are textured anisotropic materials that in some cases can be used in the production of high performance synthetic fibers. The mechanical behavior of these fibers is greatly influenced by the texture and spatial distribution of topological defects in the NLC used as a precursor. The theoretical and computational framework for the widely reported flow-induced texture and pattern formation phenomena in liquid crystal

*Corresponding author. Tel.: +1-514-398-4196. Fax: +1-514-398-6678. E-mail: alejandro.rey@mcgill.ca

Molecular Simulation
ISSN 0892-7022 print/ISSN 1029-0435 online © 2005 Taylor & Francis Group Ltd
http://www.tandf.co.uk/journals
DOI: 10.1080/08927020412331332604

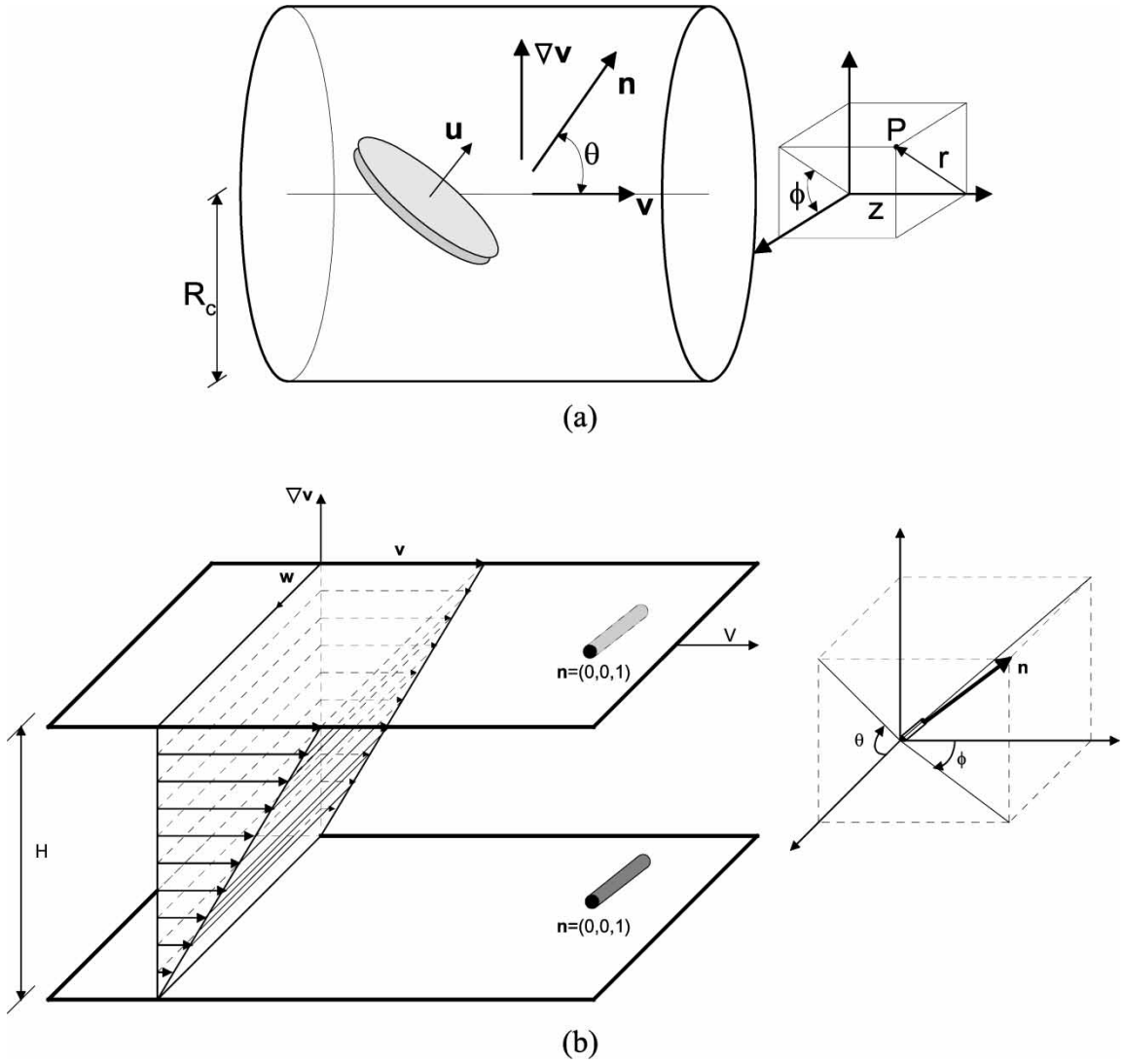

Figure 1. Definition of the flow geometry and coordinate system for capillary and simple shear flows. (a) Flow of uniaxial disk-like molecules (carbonaceous mesophases) with unit normal vector (**u**), director vector (**n**), velocity vector (**v**), velocity gradient (∇**v**), alignment tilt angle between the director and the axial direction (θ) and the cylindrical (r,ϕ,z) coordinate. (b) Simple shear flow of rod-like nematic LCPs shown the lower plate at rest, the upper plate moves with a constant velocity (V), the gap between the plates (H), director vector (**n**), and the spherical (ρ,ϕ,θ) coordinate system with the flow direction (**v**), the velocity gradient (∇**v**), the vorticity axis (**w**). The director **n** is defined by the tilt angle (θ) and the twist angle (ϕ).

materials has been investigated in several previous studies [1,2,3].

The role of shear on texture formation and texture coarsening is greatly affected by the flow properties of NLCs, the molecular weight (i.e. low-molecular weight or polymeric), the temperature and the class of NLC (i.e. lyotropic or thermotropic). The shear flow behavior and rheology of NLCs depend on the sign and magnitude of the reactive parameter λ, which is the ratio of the flow-aligning effect of the deformation rate and the tumbling (rotational) effect of the vorticity. For rod-like NLCs it is known that $\lambda > 0$ [4,5]. When $\lambda > 1$ the material flow-aligns close to the velocity direction since the rotational effect of vorticity is overcome by the aligning effect of deformation. On the other hand, when $0 < \lambda < 1$ the director does not align close to the velocity direction because the rotational effect of vorticity dominates. Rod-like nematics with $\lambda > 1$ display the flow-aligning mode, and it seems to be consensus that thermotropic nematic polymers, such as Vectra [6], are flow-aligning [7]. In contrast, for disc-like NLCs, such as carbonaceus mesophase, when $\lambda < -1$ the material is flow-aligning [5].

Macro-scale textures in carbonaceous mesophases under capillary flow consists of macroscopic modulations of the average molecular orientation and occur at insignificant values of De. Meso-scale textures of LCPs under shear consist of spatial distributions of defects that nucleate and coarsen at sufficiently high De. Inversion walls are 2D non-singular defects, in which spatially localized twist rotations occur. Once nucleated, inversion walls can shrink, pinch, or annihilate with other walls or other defects [8]. Since sheared flow-aligning nematic polymers orient very close to the velocity direction, the inversion wall formation is expected when the initial orientation is orthogonal to the

imposed flow. In this paper we use shear-induced generation of twist inversion walls as a model for texture generation in LCPs under simple shear.

Inversion walls can form loops, and can be attached to other defects or bounding surfaces. Once nucleated, inversion walls can shrink, pinch, or annihilate with other walls or other defects [8]. All these nucleation and coarsening defect processes have an impact on the viscoelastic response of the system, since elastic and dissipative mechanisms are involved. Models and theories of nucleation and coarsening of textures under flow is a topic of current interest [2,4,8]. The anisotropic properties of nematics give rise to novel field-induced re-orientation mechanisms and defect nucleation [9]. Typically, inversion walls in NLCs under external fields arise because two equivalent re-orientation (rotation) mechanisms are possible. The net result is a field-aligned sample with trapped thin layers that separate regions of clockwise rotations from those of anti-clockwise rotation.

Each class of liquid crystals displays a distinguishing number of textures. Textures exist in small-molecule nematics, both flow-aligning and tumbling [10–12], but are much more persistent in LCPs, due to the high viscosities of the latter [2]. The aim of this paper is to extend the study on flow-induced texture generation to flow-aligning thermotropic NLCs including macro, micro and meso-scale textures.

Given the dominant role of texture formation during flow processing of liquid crystalline materials a comprehensive fundamental understanding is required. This paper presents two models (Leslie–Ericksen and Landau–de Gennes) based on hierarchical multiscale computational modeling of flow-induced texture formation. The specific objectives of this paper include the elucidation of the formation of macro textures in capillary flow of carbonaceous mesophases, and the mechanism that controls textural transformation in sheared, flow-aligning, rigid-rod, nematic LCPs as function of shear rate and temperature.

This paper is organized as follows. Section 2 presents the governing equations that describe the macro-scale and micro-scale structures of carbonaceous mesophases under capillary flow and LCPs under simple shear flow, respectively. Section 3 presents numerical procedures. Section 4, presents and discusses the computational results, and Section 5 presents the conclusions.

2. Theory and governing equations

This section presents the two theories used to describe NLCs and the parametric equations used to describe texture formation. The first approach is the continuum theory due to Leslie and Ericksen [4,5], that is well adapted to describe macro-scale phenomena in low molecular weight NLCs, including carbonaceous mesophase. The second approach is the tensor order parameter theory due to Landau and de Gennes [4], that is useful to describe both micro and meso-scale phenomena and naturally describes textural defects, in LCPs.

2.1 Leslie-Ericksen theory for carbonaceous mesophases

The classical theory of elasticity of liquid crystals takes into account external forces and torques that introduce deformations in the relative molecular orientations and can distort the equilibrium configurations of the molecules. The elastic free energy density F_d a nematic uniaxial liquid crystal material is given by [4,5]:

$$F_d = \frac{K_{11}}{2}(\nabla\cdot\mathbf{n})^2 + \frac{K_{22}}{2}(\mathbf{n}\cdot\nabla\times\mathbf{n})^2 + \frac{K_{33}}{2}|\mathbf{n}\times\nabla\times\mathbf{n}|^2 \quad (1)$$

where the three basic modes of elastic storage are the splay (K_{11}), twist (K_{22}) and bend (K_{33}) modes.

The continuum theory of uniaxial nematic liquids consists of the linear and angular momentum balances, and constitutive equations for the stresses, viscous and elastic torques that takes into account external forces distort the spatially uniform equilibrium configurations of liquid crystals molecules. For incompressible isothermal conditions the general conservation of linear and angular momentum are given by the following equations [4,5]:

$$\rho\left(\frac{\partial\mathbf{v}}{\partial t} + \mathbf{v}\cdot\nabla\mathbf{v}\right) = \mathbf{f} + \nabla\cdot\boldsymbol{\sigma} \quad (2)$$

$$0 = \mathbf{G} + \mathbf{g} + \nabla\cdot\boldsymbol{\pi} \quad (3)$$

where ρ is the density, $\mathbf{v}$ is the velocity vector, $\mathbf{f}$ is the body force per unit volume vector, $\boldsymbol{\sigma}$ is the total stress, $\mathbf{G}$ is the external director body force vector, $\mathbf{g}$ is the intrinsic director body force vector, $\boldsymbol{\pi}$ is the director stress tensor, and the director inertia is neglected. Using transversely isotropic tensor coefficients, which reflect the material symmetry, the following constitutive equations for the stress tensor and the director body force were proposed by Leslie [4,5]:

$$\boldsymbol{\sigma} = -p\mathbf{I} - \frac{\partial F_d}{\partial\nabla\mathbf{n}}\cdot\nabla\mathbf{n}^T + \alpha_1(\mathbf{nn}:\mathbf{A})\mathbf{nn} + \alpha_2\mathbf{nN} + \alpha_3\mathbf{Nn} + \alpha_4\mathbf{A} + \alpha_5\mathbf{nn}\cdot\mathbf{A} + \alpha_6\mathbf{A}\cdot\mathbf{nn} \quad (4)$$

$$\mathbf{g} = a\mathbf{n} - \boldsymbol{\beta}\cdot\nabla\mathbf{n} - \frac{\partial F_d}{\partial\mathbf{n}} - \gamma_1\mathbf{N} - \gamma_2\mathbf{n}\cdot\mathbf{A} \quad (5)$$

$$\boldsymbol{\pi} = \boldsymbol{\beta}\mathbf{n} + \frac{\partial F_d}{\partial\nabla\mathbf{n}} \quad (6)$$

where

$$\mathbf{A} = (\nabla\mathbf{v} + \nabla\mathbf{v}^T)/2 \quad (7a)$$

$$\mathbf{W} = (\nabla\mathbf{v} - \nabla\mathbf{v}^T)/2 \quad (7b)$$

$$\mathbf{N} = \dot{\mathbf{n}} - \mathbf{W}\cdot\mathbf{n} \quad (7c)$$

$$\gamma_1 = \alpha_3 - \alpha_2 \quad (8a)$$

$$\gamma_2 = \alpha_6 - \alpha_5 = \alpha_3 + \alpha_2 \quad (8b)$$

$$\lambda = -\gamma_2/\gamma_1 \quad (8c)$$

p is the pressure, $\mathbf{I}$ is the unit tensor, $\{\alpha_i\}$, $i = 1\ldots6$, are the six Leslie viscosity coefficients that describes an anisotropic liquid, $\mathbf{A}$ is the rate of deformation tensor, $\mathbf{N}$ is the corotational derivative of the director vector, $\boldsymbol{\beta}$ and a are

respectively, an arbitrary vector and an arbitrary scalar used to constraint the director (**n**) to be a unit vector, γ_1 is the rotational viscosity, γ_2 is the irrotational torque coefficient, **W** is the vorticity tensor, and λ is the reactive parameter.

The director inertia is neglected in the linear momentum balance (equation (3)) because it is assumed to be insignificant in comparison to the retained viscous terms. If I is the director moment of inertia per unit volume, H is the characteristic system size, K is the average Frank elastic constant ($K = (K_{11} + K_{22} + K_{33})/3$), then the ratio of inertia to viscous effects is assumed to follow the inequality $IK/(\gamma_1 H)^2 \ll 1$. The elimination of the inertial term equation (3) is due to the fact that velocity relaxation time ($\tau_v = \rho R^2/\langle\eta\rangle$) is insignificant with respect to the orientation relaxation time ($\tau_o = \langle\eta\rangle R^2/K_{11}$) [4]. Using typical values for NLCs (for instance, $\rho = 1000\,\mathrm{kg/m^3}$, $\langle\eta\rangle = 0.1\,\mathrm{Ns/m^2}$, and $K_{11} = 10^{-11}\,\mathrm{N}$) one finds the ratio $\tau_v/\tau_o \approx 10^{-6} \ll 1$ that means the velocity field evolves much faster than the orientation field and thus it can be eliminated from the equation.

The Ericksen–Leslie theory predicts that for sufficiently large deformation rates, the director orients in the shear plane along the flow-alignment angle [4,5]. When the director field is homogeneous ($\nabla\mathbf{n} = 0$) and oriented at the alignment angle, the viscous and elastic torques vanish. For carbonaceous mesophases, the k flow-alignment stable (θ_k^s) and unstable (θ_k^u) angles exist when $\lambda < -1$ and are given by:

$$\theta_k^s = \frac{1}{2}\cos^{-1}\left(\frac{1}{\lambda}\right) + k\pi, \quad k = -1, 0, 1, 2, \ldots \tag{9a}$$

$$\theta_k^u = -\frac{1}{2}\cos^{-1}\left(\frac{1}{\lambda}\right) + k\pi, \quad k = -1, 0, 1, 2, \ldots \tag{9b}$$

Equations (9a) and (9b) show that the alignment angle of carbonaceous mesophases is not unique ($|\theta_{k+1}^s| = |\theta_k^s| + \pi$ and $|\theta_{k+1}^u| = |\theta_k^u| + \pi$). The primary alignment angle ($k = 0$) defines the primary solution for the average molecular orientation equation, denoted by P_0, and the secondary alignment angles ($k = -1, 1, 2, 3, \ldots$) define the secondary solutions for the average molecular orientation equation denoted by S_k; both classes of solutions are stable [13].

In capillary flow, using cylindrical coordinate system, and assuming that the average molecular orientation (**n**) is confined to the (r,z) plane, as shown in figure 1(a), the director vector is given by: $\mathbf{n}(r,t) = (\sin\theta(r,t), 0, \cos\theta(r,t))$. The dimensionless governing equations for the average molecular orientation tilt angle (θ) is given by [13–15]:

$$\frac{\partial\theta}{\partial t^*} = \frac{(\cos^2\theta + \varepsilon\sin^2\theta)}{Y^*(\theta)}\left(\frac{\partial^2\theta}{\partial r^{*2}} + \frac{1}{r^*}\frac{\partial\theta}{\partial r^*}\right) + \frac{\sin 2\theta}{2Y^*(\theta)}\left[(\varepsilon - 1)\left(\frac{\partial\theta}{\partial r^*}\right)^2 - \frac{1}{r^{*2}}\right] - \left[\frac{U^*(\theta)\mathrm{Er}}{2G^*(\theta)Y^*(\theta)}\right]r^* \tag{10}$$

$$\frac{\partial v^*}{\partial r^*} = -\left(\frac{r^*}{2G^*(\theta)}\right)\mathrm{Er} + \left(\frac{U^*(\theta)}{G^*(\theta)}\right)\frac{\partial\theta}{\partial t^*} \tag{11}$$

$$Y^*(\theta) = \gamma_1^* - \frac{U^{*2}(\theta)}{G^*(\theta)} \tag{12}$$

$$G^*(\theta) = \alpha_1^*\sin^2\theta\cos^2\theta + \frac{(\alpha_5^* - \alpha_2^*)}{2}\sin^2\theta + \frac{(\alpha_3^* + \alpha_6^*)}{2}\cos^2\theta + \frac{\alpha_4^*}{2} \tag{13}$$

$$U^*(\theta) = \alpha_2^*\sin^2\theta - \alpha_3^*\cos^2\theta \tag{14}$$

where α_i^* are the dimensionless Leslie viscosities ($\alpha_i^* = \alpha_i/\langle\eta\rangle$), $\langle\eta\rangle$ is the average Miesowicz viscosity [13,15], $\varepsilon = K_{33}/K_{11}$ is the ratio of the bend and the splay Frank elastic constants, $\mathrm{Er} = R_c^3(-\mathrm{d}p/\mathrm{d}z)/K_{11}$ is the ratio of viscous flow effects to long-range elasticity effects known as the Ericksen number (Er), $r^* = r/R_c$ is the dimensionless radius, R_c is the capillary radius, $t^* = K_{11}t/(R_c^2\langle\eta\rangle)$ is the dimensionless time, $-\mathrm{d}p/\mathrm{d}z$ is the given pressure drop in the capillary per unit length, $Y^*(\theta)$ is the dimensionless re-orientation viscosity and $U^{*2}(\theta)/G^*(\theta)$ is the dimensionless backflow viscosity function. The last term on equation (10) represents the viscous torques acting on the director.

2.2 *Landau-de Gennes theory for liquid crystal polymers*

This theory is well suited to simulate meso-scale texture formation in nematic LCPs. The microstructure of the thermotropic liquid crystal polymer is described conveniently in terms of a second order, symmetric and traceless tensor order parameter **Q** [4]:

$$\mathbf{Q} = \int_{Z^2}\left(\mathbf{uu} - \frac{\mathbf{I}}{3}\right)f(\mathbf{u})\,\mathrm{d}A \tag{15}$$

where **u** is the unit vector normal to the rod-like molecules, Z^2 denotes the unit sphere, **I** is second order unit tensor, $f(\mathbf{u})$ is the orientation distribution function, and $\mathrm{d}A$ is the differential area in spherical coordinates. Alternatively **Q** can also be defined in terms of three eigenvectors (**n**, **m** and **l**) and three eigenvalues ($\lambda_\mathbf{n}$, $\lambda_\mathbf{m}$ and $\lambda_\mathbf{l}$):

$$\mathbf{Q} = \lambda_\mathbf{n}\mathbf{nn} + \lambda_\mathbf{m}\mathbf{mm} + \lambda_\mathbf{I}\mathbf{ll} \tag{16}$$

The eigenvalues can be presented as functions of the scalar order parameter S and the biaxial order

parameter P [12]:

$$\lambda_{\mathbf{n}} = \frac{2}{3}S, \quad \lambda_{\mathbf{m}} = \frac{1}{3}(P - S), \quad \lambda_{\mathbf{l}} = -\frac{1}{3}(P + S) \tag{17}$$

with the restriction:

$$\lambda_{\mathbf{n}} + \lambda_{\mathbf{m}} + \lambda_{\mathbf{l}} = 0 \tag{18}$$

The governing equations for liquid crystal flows follow from the dissipation function (Δ) given by:

$$\Delta = \mathbf{t}^s : \mathbf{A} + ckT\mathbf{H} : \hat{\mathbf{Q}} \tag{19}$$

where $\mathbf{t}^s$ is the viscoelastic stress tensor, $\mathbf{A}$ is the symmetric traceless rate of deformation tensor (given by equation (7a)), c is the concentration of molecules per unit volume, k the Boltzmann constant, T the absolute temperature, $\mathbf{H}$ is the molecular field, and $\hat{\mathbf{Q}}$ is the Jaumann derivative of the tensor order parameter, given by:

$$\hat{\mathbf{Q}} = \frac{\partial \mathbf{Q}}{\partial t} + (\mathbf{v}\cdot\nabla)\mathbf{Q} - \mathbf{W}\cdot\mathbf{Q} + \mathbf{Q}\cdot\mathbf{W} \tag{20a}$$

$$(ckT)\mathbf{H} = -\left(\frac{\delta F}{\delta \mathbf{Q}}\right)^{[s]} = \left(\frac{\partial f}{\partial \mathbf{Q}} - \nabla\cdot\frac{\partial f}{\partial \nabla\mathbf{Q}}\right)^{[s]} \tag{20b}$$

where $\mathbf{W}$ is the vorticity tensor (given by equation (7b)) and F is the total free energy; f is the free energy density that is given by:

$$\begin{aligned} f = (ckT)\Bigg\{&\frac{1}{2}\left(1 - \frac{1}{3}U\right)\mathbf{Q} : \mathbf{Q} - \frac{1}{3}U\mathbf{Q} : (\mathbf{Q}\cdot\mathbf{Q}) \\ &+ \frac{1}{4}U(\mathbf{Q} : \mathbf{Q})^2 + \frac{L_1}{2ckT}\left[\nabla\mathbf{Q} : (\nabla\mathbf{Q})^T\right] \\ &+ \frac{L_2}{2ckT}(\nabla\cdot\mathbf{Q})\cdot(\nabla\cdot\mathbf{Q})\Bigg\} \end{aligned} \tag{21}$$

where, $U = 3T^*/T$ is the nematic potential, T^* is the isotropic-nematic transition temperature, L_1 and L_2 are the Landau coefficients, and the superscript [s] denotes symmetric and traceless. Using the Landau–de Gennes free energy density, the molecular field is given by:

$$\begin{aligned} -\left(\frac{\delta F}{\delta \mathbf{Q}}\right)^{[s]} &= ckT\mathbf{H} \\ &= -ckT\Bigg\{\left(1 - \frac{1}{3}U\right)\mathbf{Q} - U\mathbf{Q}\cdot\mathbf{Q} \\ &\quad + U\left[(\mathbf{Q} : \mathbf{Q})\mathbf{Q} + \frac{1}{3}(\mathbf{Q} : \mathbf{Q})\mathbf{I}\right]\Bigg\} \\ &\quad + ckT\Bigg(\frac{L_1}{ckT}\nabla^2\mathbf{Q} + \frac{1}{2}\frac{L_2}{ckT} \\ &\quad \cdot\left\{\nabla(\nabla\cdot\mathbf{Q}) + \left[\nabla(\nabla\cdot\mathbf{Q})\right]^T - \frac{2}{3}tr[\nabla(\nabla\cdot\mathbf{Q})]\mathbf{I}\right\}\Bigg) \end{aligned} \tag{22}$$

and contains both short range and long range contributions. Expanding the forces ($\mathbf{t}^s$,$\hat{\mathbf{Q}}$) in terms of fluxes ($\mathbf{A}$, $ckT\mathbf{H}$), and taking into account thermodynamic restrictions and the symmetry and tracelessness of the forces and fluxes, equations for $\mathbf{t}^s$ and $\hat{\mathbf{Q}}$ can be obtained. The dynamics of the tensor order parameter is given by the following sum of flow $\mathbf{F}$, short range $\mathbf{H}^{sr}$, and long range $\mathbf{H}^{lr}$ contributions [12]:

$$\hat{\mathbf{Q}} = \mathbf{F}(\mathbf{Q}, \nabla\mathbf{v}) + \mathbf{H}^{sr}[\mathbf{Q}, \overline{D}_r(\mathbf{Q})] + \mathbf{H}^{lr}(\nabla\mathbf{Q}) \tag{23}$$

(i) Flow contribution $\mathbf{F}$:

$$\begin{aligned} \mathbf{F}(\mathbf{Q}, \nabla\mathbf{v}) = &\frac{2}{3}\beta\mathbf{A} + \beta\left[\mathbf{A}\cdot\mathbf{Q} + \mathbf{Q}\cdot\mathbf{A} - \frac{2}{3}(\mathbf{A} : \mathbf{Q})\mathbf{I}\right] \\ &- \frac{1}{2}\beta\{(\mathbf{A} : \mathbf{Q})\mathbf{Q} + \mathbf{A}\cdot\mathbf{Q}\cdot\mathbf{Q} + \mathbf{Q}\cdot\mathbf{A}\cdot\mathbf{Q} \\ &+ \mathbf{Q}\cdot\mathbf{Q}\cdot\mathbf{A} - [(\mathbf{Q}\cdot\mathbf{Q}) : \mathbf{A}]\mathbf{I}\} \end{aligned} \tag{24}$$

(ii) Short-range elastic contribution $\mathbf{H}^{sr}$:

$$\begin{aligned} \mathbf{H}^{sr}[\mathbf{Q}, \overline{D}_r(\mathbf{Q})] = -6\overline{D}_r\Bigg\{&\left(1 - \frac{1}{3}U\right)\mathbf{Q} - U\mathbf{Q}\cdot\mathbf{Q} \\ &+ U\left[(\mathbf{Q} : \mathbf{Q})\mathbf{Q} + \frac{1}{3}(\mathbf{Q} : \mathbf{Q})\mathbf{I}\right]\Bigg\} \end{aligned} \tag{25}$$

(iii) Long-range elastic contribution $\mathbf{H}^{lr}$:

$$\begin{aligned} \mathbf{H}^{lr}(\nabla\mathbf{Q}) = 6\overline{D}_r\Bigg(&\frac{L_1}{\mathrm{ckT}}\nabla^2\mathbf{Q} + \frac{1}{2}\frac{L_2}{ckT}\Bigg\{\nabla(\nabla\cdot\mathbf{Q}) \\ &+ [\nabla(\nabla\cdot\mathbf{Q})]^T - \frac{2}{3}tr[\nabla(\nabla\cdot\mathbf{Q})]\mathbf{I}\Bigg\}\Bigg) \end{aligned} \tag{26}$$

$$\overline{D}_r = \frac{D_r}{1 - \frac{3}{2}\mathbf{Q} : \mathbf{Q}} \tag{27}$$

where $\overline{D}_r$ is the microstructure dependent rotational diffusivity, D_r is the pre-averaged rotational diffusivity here taken to be constant and β is a thermodynamic parameter that is unrestricted, because it introduces couplings between fields of opposite time reversal.

The dimensionless form of the governing equation for the tensor order parameter $\mathbf{Q}$ is:

$$\begin{aligned} Er\hat{\mathbf{Q}}^* = Er\Bigg(&\frac{2}{3}\beta\mathbf{A}^* + \beta\left[\mathbf{A}^*\cdot\mathbf{Q} + \mathbf{Q}\cdot\mathbf{A}^* - \frac{2}{3}(\mathbf{A}^* : \mathbf{Q})\mathbf{I}\right] \\ &- \frac{1}{2}\beta\Bigg\{(\mathbf{A}^* : \mathbf{Q})\mathbf{Q} + \mathbf{A}^*\cdot\mathbf{Q}\cdot\mathbf{Q} + \mathbf{Q}\cdot\mathbf{A}^*\cdot\mathbf{Q} + \mathbf{Q}\cdot\mathbf{Q}\cdot\mathbf{A}^* \\ &- [(\mathbf{Q}\cdot\mathbf{Q}) : \mathbf{A}^*]\mathbf{I}\Bigg\}\Bigg) - \frac{3}{U}\cdot\frac{R}{\left(1 - \frac{3}{2}\mathbf{Q} : \mathbf{Q}\right)^2} \\ &\cdot\Bigg\{\left(1 - \frac{1}{3}U\right)\mathbf{Q} - U\mathbf{Q}\cdot\mathbf{Q} \\ &+ U\left[(\mathbf{Q} : \mathbf{Q})\mathbf{Q} + \frac{1}{3}(\mathbf{Q} : \mathbf{Q})\mathbf{I}\right]\Bigg\} \\ &+ \frac{3}{\left(1 - \frac{3}{2}\mathbf{Q} : \mathbf{Q}\right)^2}\Bigg(\nabla^{*2}\mathbf{Q} + \frac{1}{2}L_2^*\Bigg\{\nabla^*(\nabla^*\cdot\mathbf{Q}) \\ &+ [\nabla^*(\nabla^*\cdot\mathbf{Q})]^T - \frac{2}{3}tr[\nabla^*(\nabla^*\cdot\mathbf{Q})]\mathbf{I}\Bigg\}\Bigg) \end{aligned} \tag{28}$$

where $t^* = \dot{\gamma} t$, $\mathbf{A}^* = \frac{\mathbf{A}}{\dot{\gamma}}$, $\mathbf{W}^* = \frac{\mathbf{W}}{\dot{\gamma}}$, $\nabla^* = H\nabla$, $L_2^* = \frac{L_2}{L_1}$ are the dimensionless quantities, and $\dot{\gamma}$ is a characteristic shear rate. The Er, which is the dimensionless ratio between viscous flow effects, the characteristic viscosity (η), and long-range order elasticity and the energy ratio (R), which is the dimensionless ratio between short-range order elasticity and long-range order elasticity, are given by [16]:

$$\mathrm{Er} = \frac{\dot{\gamma} H^2 \eta}{L_1} \tag{29a}$$

$$\eta = \frac{ckT^*}{2D_r} \tag{29b}$$

$$R = \frac{3H^2 ckT^*}{L_1} \tag{29c}$$

The De, which is the ratio between flow effect and short range energy effect, is given by:

$$\mathrm{De} = \frac{\mathrm{Er}}{R} = \frac{\dot{\gamma}}{6D_r} \tag{30}$$

and its magnitude controls the amplitude of effects associated with the scalar order parameters.

The Landau–de Gennes model for nematic liquid crystals has an external length scale l_e and an internal length scale l_i as follows:

$$\ell_e = H, \quad \ell_i = \sqrt{\frac{L_1}{3ckT^*}}, \quad \ell_e \gg \ell_i \tag{31}$$

It should be noted that the external length scale governs the directors' orientation ($\mathbf{n}, \mathbf{m}, \mathbf{l}$) while the internal length scale governs the scalar order parameter (S,P). The external τ_e and internal τ_i time scales of model are ordered as follows:

$$\tau_e = \frac{\eta H^2}{3L_1}, \quad \tau_i = \frac{1}{D_r}, \quad \tau_e \gg \tau_i \tag{32}$$

The external time scale describes slow orientation variations and the internal length scale describes fast order parameter variations. Finally the presence of shear flow of rate γ introduces a flow time scale τ_f:

$$\tau_f = \frac{1}{\dot{\gamma}} \tag{33}$$

and a flow length scale ℓ_f :

$$\ell_f = \sqrt{\frac{\delta}{\dot{\gamma}}}, \quad \delta = \frac{L_1}{\eta} \tag{34}$$

where δ is the orientation diffusivity.

In the micro texture section, the simple start-up shear flow of a nematic liquid crystal polymer, as shown in figure 1(b), will be discussed; note that in this flow the lower plate is fixed and the upper plate starts moving at $t = 0$ with a known constant velocity (V).

3. Computational methods

3.1 Leslie–Ericksen model for carbonaceous mesophase

For the macro-scale texture study, using the Leslie–Ericksen theory, the average orientation equation (10) is solved numerically using the Galerkin Finite Element method for spatial discretization and the finite differences method for time discretization. All integrals were computed using three-point Gaussian quadrature, and the resulting set of non-linear equations was solved using the Newton–Raphson iteration scheme. In the steady-state simulations the zero order continuation method was employed. In all time-dependent simulations the spatial discretization used 500 linear elements and a uniform mesh, while for time integration we used fourth order explicit Runge–Kutta method with a fixed time step of 10^{-8}. The mesh independence was established using standard mesh refinement criteria. These simulations were carried out using the parameters that correspond to the Frank elastic constants measured for a well-characterized discotic nematic, hexakis(dodecanoyloxy)truxene, and the six scaled Leslie coefficients calculated from non-equilibrium molecular dynamics simulations [13–15,17]; however, the results discussed here for discotic NLCs are independent of the exact values of the viscoelastic parameters and arise whenever the reactive parameter (λ) is less than minus one. The average molecular orientation in the center of the capillary is assumed as planar, and in the capillary wall three values are assumed: (a) planar, (b) $\pi - 1.39$ or (c) $\pi - 2.43$ radians; in addition, the no slip condition is assumed for the velocity at the capillary wall. The boundary conditions in this case are:

$$\theta(0, t^*) = 0 \tag{35a}$$

$$\theta(1, t^*) = 0 \text{ or } \pi - 1.39 \text{ or } 2.43 - \pi \tag{35b}$$

$$v^*(1, t^*) = 0 \tag{35c}$$

3.2 Landau–de Gennes model for liquid crystal polymers

The meso-scale model given by equation (28), actually is a set of five coupled non-linear parabolic partial differential equations, which are solved using the Galerkin Finite Elements Method for spatial discretization and the fourth order Runge–Kutta time adaptive method. Convergence and mesh-independence were established in all cases using standard methods. Spatial discretization was judiciously selected taking into account the length scale of our model. The selected adaptive time integration scheme is able to efficiently take into account the stiffness that rises due to

the disparity between time scale: $\tau_i \ll \tau_e$. The boundary conditions in this case are:

$$\mathbf{Q}_s(y^* = 0) = \mathbf{Q}_s(y^* = 1) = S_{eq}\left(\mathbf{n}_s\mathbf{n}_s - \frac{\mathbf{I}}{3}\right) \quad (36a)$$

$$\mathbf{n}_s = (0, 0, 1) \quad (36b)$$

$$S_{eq} = \frac{1}{4} + \frac{3}{4}\sqrt{1 - \frac{8}{3U}} \quad (36c)$$

describing fixed director orientation along the vorticity axis, a uniaxial state with the scalar order parameter equal to its equilibrium value. The initial state is assumed to be uniaxial and at equilibrium. The thermodynamic parameter β and the nematic potential U are used to calculate the reactive parameter λ, which indicates if the system is flow-aligning or not. In the micro-texture section the values for these parameters are chosen to assure that the rod-like NLC is flow-aligning $(\lambda > 1)$: $\beta = 1.2,\ 2.75 < U < 4.5$. The selected ranges for the dimensionless parameters are: $R = 10^6,\ 0 < \mathrm{De} < 6$.

4. Numerical results

The macro-scale texture of liquid crystalline materials is a low De process that can be described by the average molecular orientation given by the director vector, well described by the Leslie–Ericksen model. In contrast, the meso-scale texture of these materials is an arbitrary De process that includes a molecular and an orientational process; as a result, these textures must be simulated using the Landau–de Gennes model.

4.1 Macro scale textures in carbonaceous mesophases

4.1.1 Steady-state simulations. The texture formation due to purely elastic effects fails to capture the length scale gradients shown in real fibers produced from liquid crystals precursors [18]. This section presents the macro texture formation, which is driven by flow effects, and retains the elastic effects. The length scale distribution in the predicted flow-induced texture, in contrast to the elastic-induced texture, is consistent with the experimental data [14,18].

As explained in [13] the solutions of equations (10) and (11) can be classified as primary (P_k), secondary (S_k) and hybrid ($H_{k-1,k}$ or $H_{k,k+1}$). The P_k exists for all values of Er, the S_k exists above a critical value of Er, and the $H_{k-1,k}$ or $H_{k,k+1}$ exists only for some specific values of anchoring angle at the capillary wall and are not stable.

The average molecular orientation, obtained from equation (10), as a function of dimensionless radial distance for high Er for the primary ($k = 0$) and the selected secondary solutions ($S_k : k = -1, 1, 2, 3, \ldots$) shows that higher order solutions exhibit a narrow alignment region in between core and rim regions over which the director vector exhibits also the same orientation periodically. On the other hand, the low order solutions exhibit alignment over a wide annular region and narrow core and rim regions.

The solution multiplicity helps to explain macro-textural phenomena, such a multiple concentric ring formation, found in the flow of carbonaceous mesophases. The solution multiplicity is a function of the Er and the anchoring angle at the capillary wall; at some specific values of anchoring angle primary, secondary and hybrid solutions can coexists (see more details in [13]).

Figure 2 shows the computed texture visualization of the orientation field cross sections for the principal (P_0), secondary (S_1 and S_{-1}) and hybrid solutions ($H_{1,0}$ and $H_{-1,0}$) for two anchoring angle at the wall: $\theta^w = \pi - 1.39$ radians (left side column) and $\theta^w = 2.43 - \pi$ radians (right side column); the Er is 1000 in both cases [12]. Black stands for full alignment orientation ($\theta_k^s = \theta_0^s + k\pi$ radians, where k is an integer that gives the order of the secondary solution and θ_0^s is the first alignment angle, 1.157 radians in the present case) and white stands for non-alignment ($\theta_k^u = \theta_0^u + k\pi$ radians, where θ_0^u is the first unstable angle, 1.985 radians in the present case); the figures show the three families of textures that coexists.

Figure 3 shows the computed texture visualization of the average molecular orientation profile for primary and selected secondary solutions ($S_k : k = -1, 4, 5, 9, 14, 16$). The orientation profiles for the secondary solutions give a ring texture with a characteristic ring thickness that is a function of position. The figures show that the number of rings is equal to the order of the solution. For example the $k = 4$ solution has four rings, $k = 5$, solution has five rings and so on. For secondary solutions all textures have three regions: a small core region surrounding the fiber axis, a large ring (black band) in the central annular region, and an outer rim region dense with thin rings. As k increases the width of the annular region decreases and the number of rings in the rim region increases. Note that as the order of the solution (k) increases, thinner rings appear close to the rim, which are consistent with experiments. The rim region has a thin structural length scale, while the core region has a large structural length scale. The origin of the texture length scale is set by the orientation gradient length scale. For higher order solutions, as the director rotates from (θ^s) to zero, the texture length scale is set by the magnitude of the orientation gradient.

The previous discussion took into consideration the role of higher order solutions on the generation of the ring texture, now we consider the role of the pressure drop on the texture length scale. The average molecular orientation (θ) as a function of the dimensionless radial distance for the secondary solutions shows that as the Er increases the aligned annular region increases, and the rim region exhibits sharper and sharper gradients. The core region remains almost unaffected by pressure drop increases. Figure 4 shows the texture visualization of solutions S_{+4}, and S_{+5} for Ers: 2728 or 3310, 5000, and 10,000. Again, in this plot black corresponds to the full alignment

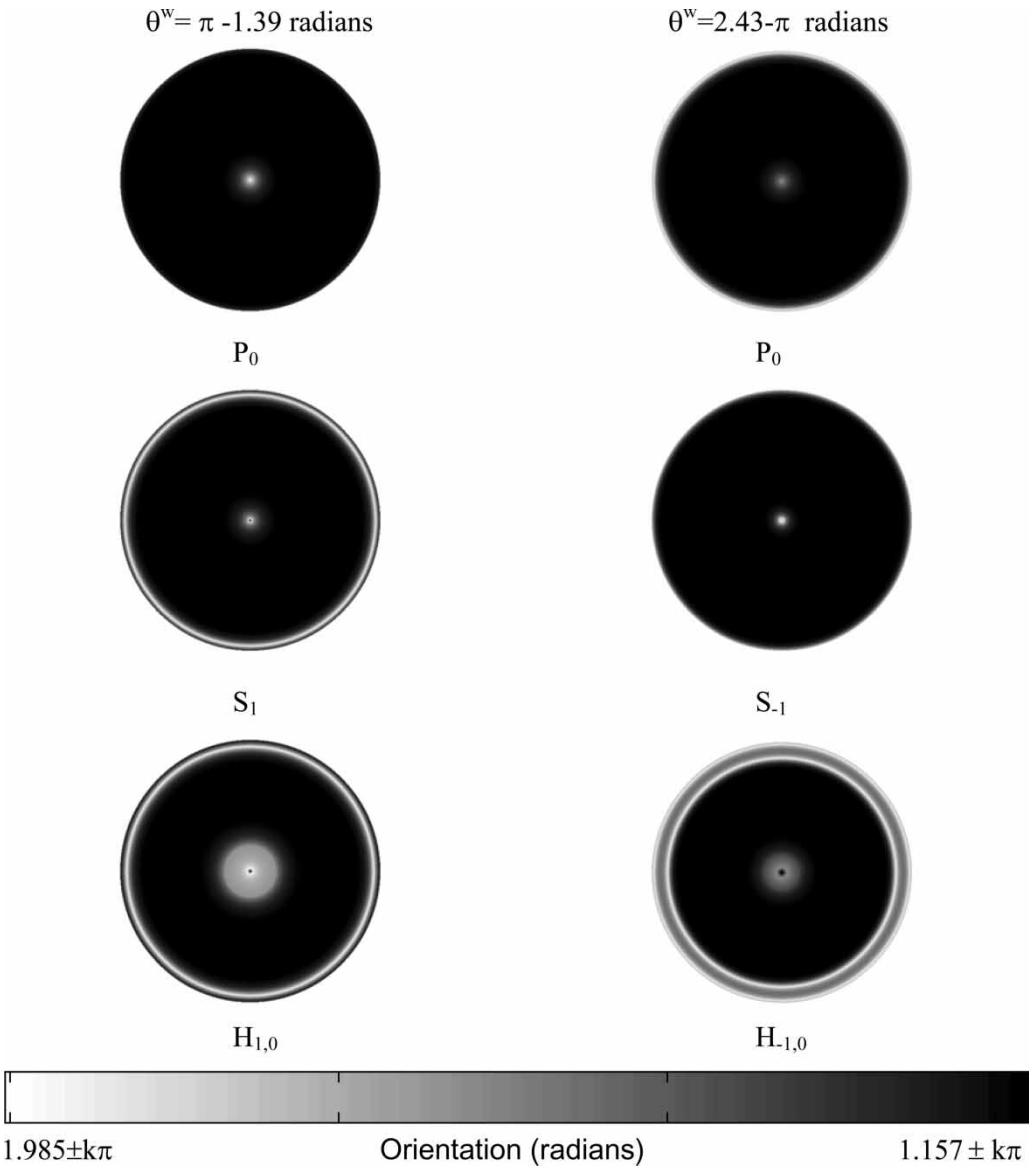

Figure 2. Computed texture visualization of the NLC cross sections to the principal (P_0), secondary (S_1 and S_{-1}) and hybrid solutions ($H_{1,0}$ and $H_{-1,0}$) for two anchoring angle at the wall: $\theta^w = -1.39 + \pi$ radians (left column) and $\theta^w = 2.43 - \pi$ radians (right column); Er = 1000 in both cases. Black stands for full alignment with the stable Leslie angle and white stands for non-alignment.

orientation (radians, where k is an integer that gives the order of the secondary solution and is the first alignment angle, 1.157 radians in the present case) and white corresponds to the non-alignment orientation ($\theta_k^u = \theta_0^u + k\pi$ radians, where θ_0^u is the first unstable angle, 1.985 radians in the present case). The figure shows that in both cases as the Er increases, the number of rings remains constant, but they move towards the rim. The picture shows that as the Er increases the ring thickness decreases, and the rings pile up at the rim. These predictions agree with the fact that as the higher shear rates close to the wall, it will refine the texture length scale. The pressure drop has almost no effect at the core because at the center the shear rate vanishes and the structure remains unaffected by the flow. Thus lower pressure drops produce more uniform textures than larger pressure drops. Since the number of rings remains constant, an increase in the annular region will result in compression of the rim region.

4.1.2 Transient simulations. The time evolution of the average molecular orientation profiles shows that the solution evolves towards the primary solution P_0. Figure 5 shows for Er 2500, and initial condition $\theta(r^*) = 0$, the texture visualization of the fiber cross-section time evolution. Black stands for full alignment orientation and white stands for non-alignment.

The time evolution of the average molecular orientation profile when the initial conditions is bounded by $\theta_0^u \leq \theta(r^*) \leq \theta_2^u$ and the Er sufficiently large, shows that the final average molecular orientation profile is given by secondary solution S_{+1}. Figure 6 shows the texture visualization of the fiber cross-section time evolution for Ericksen (Er) number 2500 and initial conditions

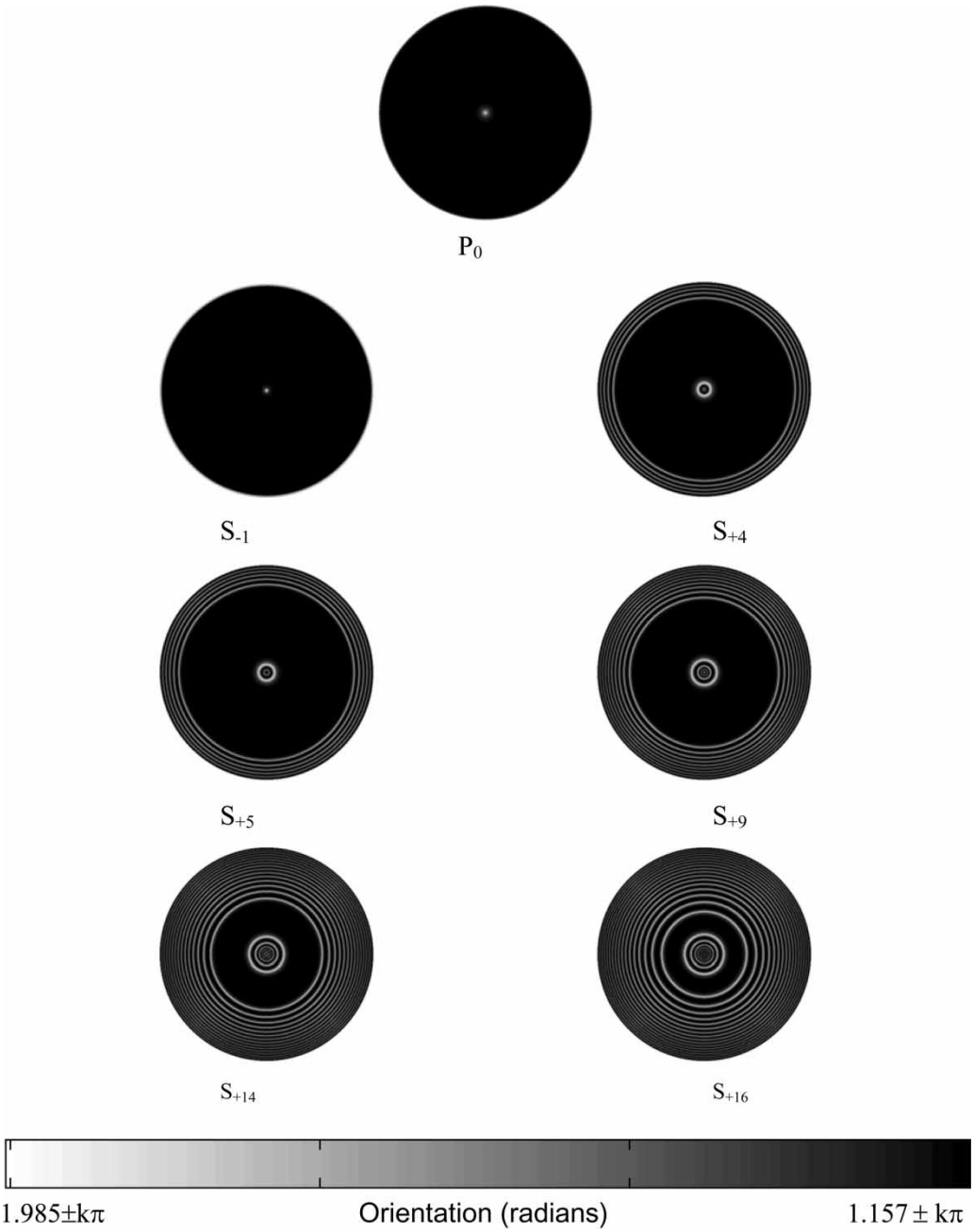

Figure 3. Computed cross-section macro-texture visualization for the principal (P_0) and selected secondary solutions ($S_{k:k=-1,+4,+5,+9,+14,+16}$) of carbonaceous mesophases under capillary flow. The Er number is 10,000. Black stands for full alignment with the stable Leslie angle and white stands for non-alignment.

$\theta(r^*) = 2.5 \sin(\pi r^*)^{0.4}$. Black stands for full alignment and white stands for non-alignment.

4.2 Meso-scale texture in liquid crystal polymers

Previous work for simple shear flow [19] has shown that as the Er number increases, the Landau–de Gennes theory predicts the existence of six stable steady state modes, as follows:

(i) Homogeneous mode (H): the director is aligned everywhere along the vorticity axis ($n_z = 1$).

(ii) Symmetric mode (S): the director reorients uniformly towards the shear plane, creating a symmetric twist angle profile. Since the reorientation has a unique sense (say clockwise) no twist wall appears at the center region.

(iii) Asymmetric mode (A): the re-orientation direction in the top half-layer is opposite to the bottom half-layer. The resulting director field exhibits a twist wall at the center of the gap, and two boundary layers at the bounding surfaces.

(iv) Defect lattice mode (DL): The number of re-orientation reversal increases with increasing shear rate, and

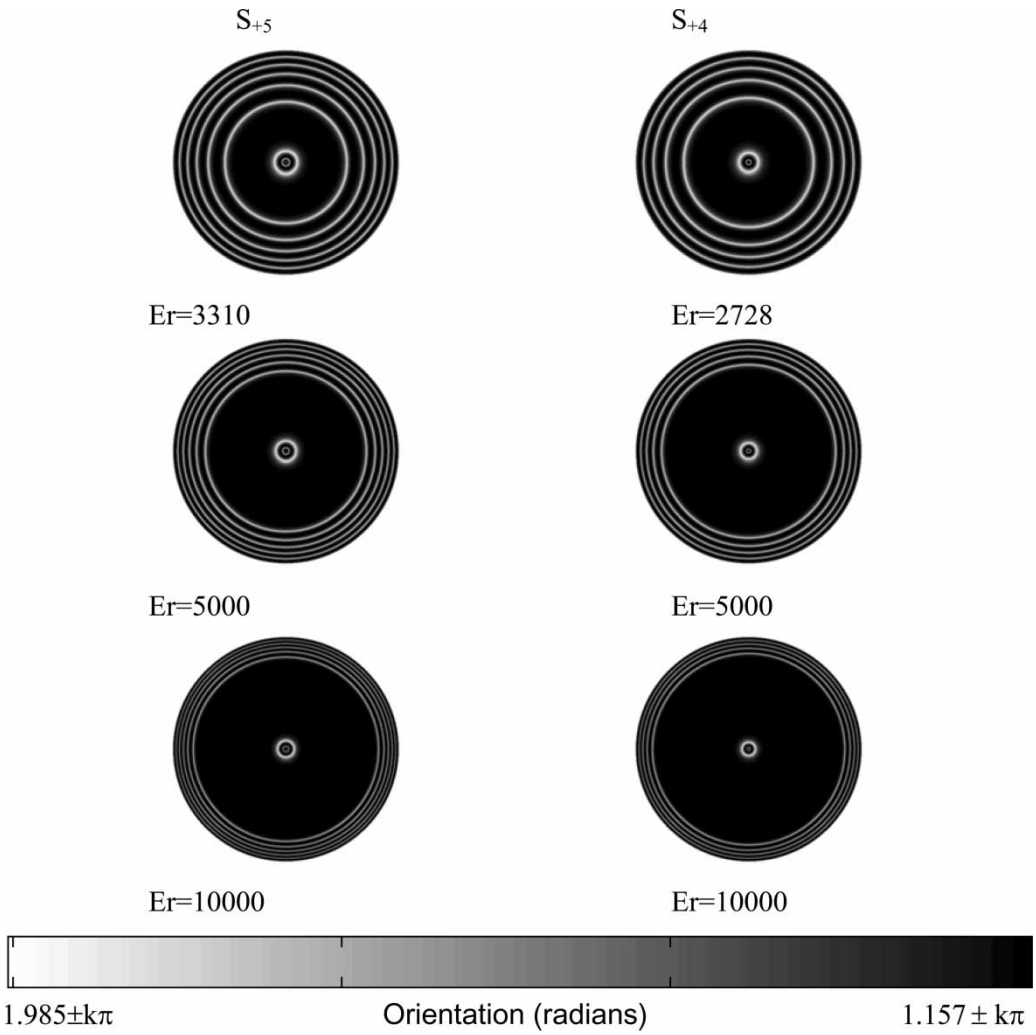

Figure 4. Computed cross-section macro-texture visualization for secondary solutions S_{+4} and S_{+5} of carbonaceous mesophases under capillary flow, for three values of Er number: the critical value (2728 for S_{+4} and 3310 for S_{+5}), 5000 and 10,000. Black stands for full alignment with the stable Leslie angle and white stands for non-alignment.

the director field displays a finite number of twist inversion walls separated by a nearly constant distance. The mode is spatially periodic and the wave-length is the wall–wall distance. Since the mode is periodic it is denoted defect lattice.

(v) Defect gas mode (DG): In this mode, annihilation processes set in and walls nucleate and react with other walls, with the bounding surfaces, and/or they pinch. Since coarsening is a random process it destroys periodicity and the mode is referred as a defect gas mode. The twist wall distance is a random variable.

(vi) Planar mode (P): At the highest shear rates, annihilation by pinching overcomes defect nucleation, and no twist walls remain at steady state. The resulting mode is planar and defect-free.

It is found [19] that the texture transition cascade: unoriented monodomain $\Rightarrow$ defect lattice $\Rightarrow$ defect gas $\Rightarrow$ oriented monodomain is remarkably consistent with the textural transition of sheared lyotropic tumbling nematic polymers [20].

Since the governing time scales at high shear rates are the flow time scale (see equation (33)), all transient results are plotted as a function of strain $\gamma = \dot{\gamma}t$. In the following, we will present results for the last three modes.

Figure 7 shows computed gray scale visualizations of director component n_z $(0 \leq y^* \leq 1)$ as a function of strain, corresponding to the three modes: (a) DL (De $= 0.05$, $U = 4.5$, $R = 10^6$); (b) DG (De $= 2.4$, $U = 4.25$, $R = 10^6$) and (c) planar P mode (De $= 4.6$, $U = 4.5$, $R = 10^6$). Black represents in plane orientation ($n_z = 0$) and light represents orientation along the vorticity ($n_z = 1$) axis.

The steady state texture of a liquid crystal is given by the balance of nucleation and coarsening processes. Coarsening events limit the lifetime of an inversion wall, and a texture can be viewed as a balance between birth–death events. Coarsening processes of inversion

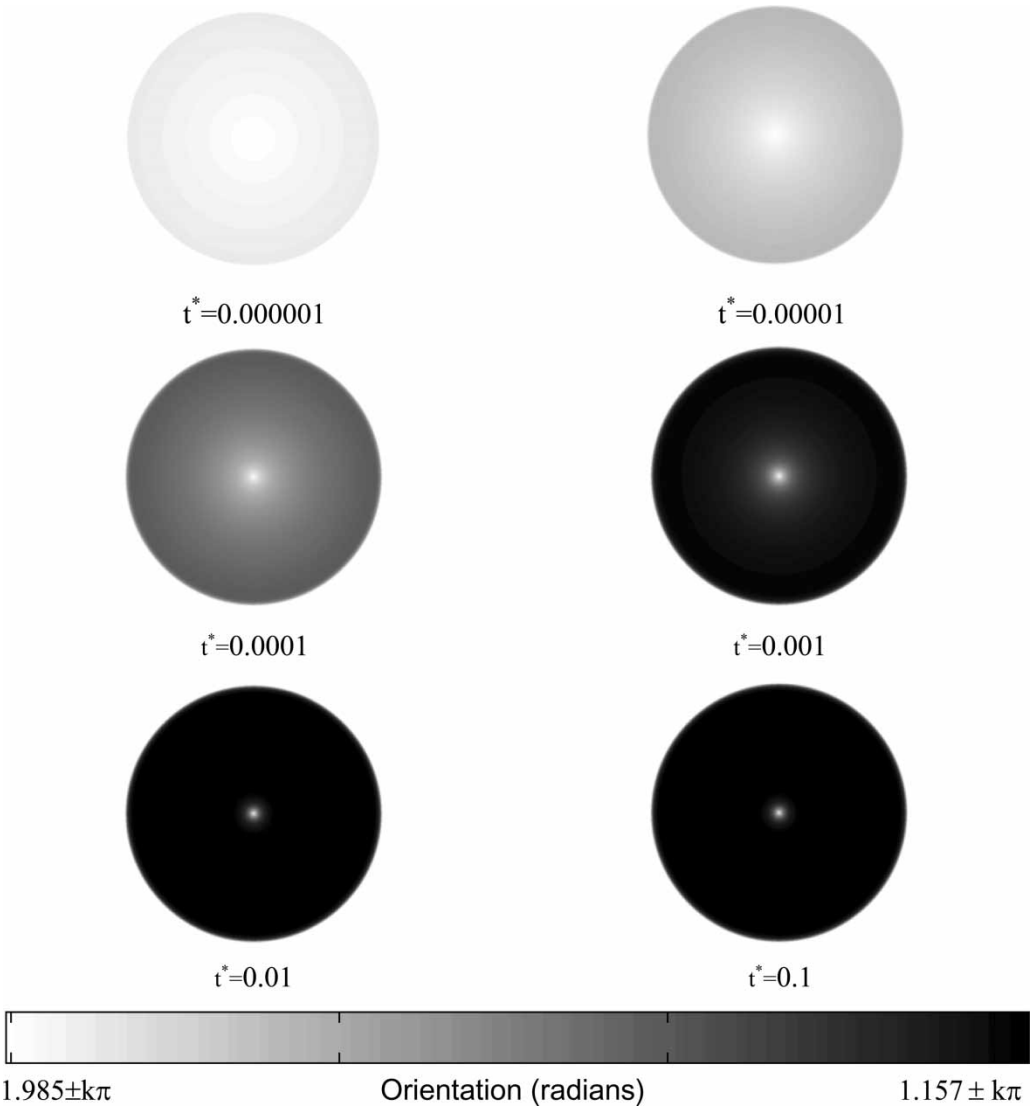

Figure 5. Time evolution of macro-texture visualization for primary solution (P_0) and Er = 2500, for carbonaceous mesophases under capillary flow. Black stands for full alignment with the stable Leslie angle and white stands for non-alignment.

walls under shear can involve: (a) wall-bounding surface reaction, (b) wall–wall annihilation and (c) pinching [19].

Figure 8(a) shows a computed visualization of director component n_z $(0 \leq y^* \leq 1)$ as a function of strain for $R = 10^6$, $U = 4$, De = 0.01, corresponding to wall–bounding surface interaction in the defect lattice mode. Black represents in plane orientation ($n_z = 0$) and light orientation along the vorticity ($n_z = 1$). As strain increases, one wall is absorbed by the bounding surface leaving behind a single wall in the bulk. Figure 8(a) is a unique example of a defect–bounding surface interaction. Models of surface defect emission have been postulated [21], and also observed experimentally [9] but never simulated with the classical nematodynamics equations. Figure 8(b) shows a computed visualization of director component n_z $(0 \leq y^* \leq 1)$ as a function of strain, for $R = 10^6$, $U = 3$, De = 0.04, corresponding to wall–wall interaction in the DL mode. Black represents in plane orientation ($n_z = 0$) and light represents orientation along the vorticity ($n_z = 1$) axis. As strain increases, the walls annihilate leaving behind a planar director field. Figure 8(c) shows a computed visualization of director component n_z $(0 \leq y^* \leq 1)$ as a function of strain for $R = 10^6$, $U = 3.5$, De = 0.83, corresponding to wall pinching in the planar mode. Black represents in plane orientation ($n_z = 0$) and light orientation along the vorticity ($n_z = 1$). As strain increases the walls pinch separately leaving behind a planar director field.

Figure 9 shows the number of inversion walls at steady state function of shear rate (De) for different temperatures (nematic potential, U) for $R = 10^6$, $\beta = 1.2$. The number of nucleated inversion walls increases when the temperature decreases (U increases).

Figure 10 shows the texture modes of thermotropic LCPs in the temperature (U)–shear rate (De) plane, for

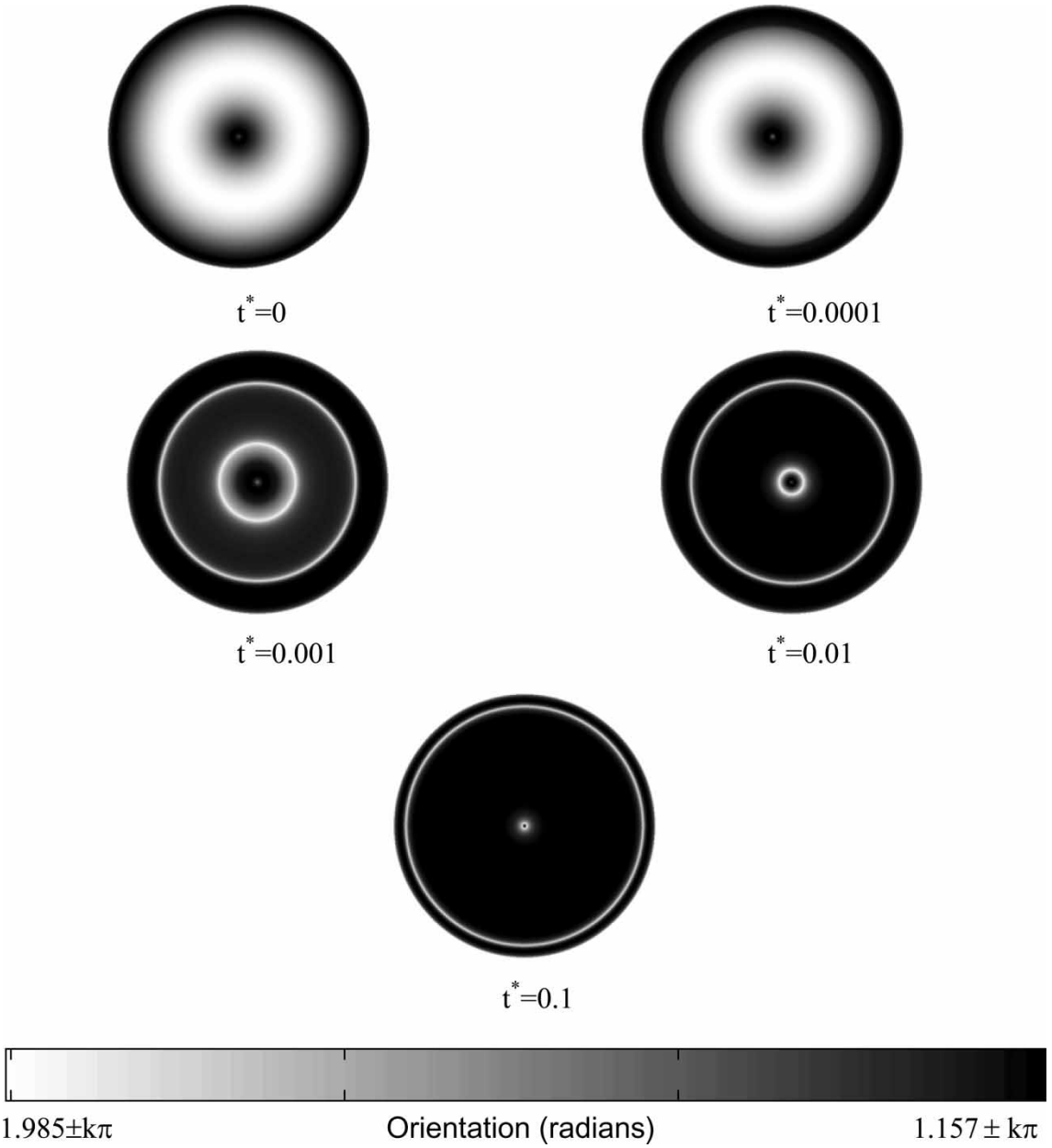

Figure 6. Time evolution of macro-texture visualization for the secondary solution (S_{+4}) and Er = 2500, for carbonaceous mesophases under capillary flow. Black stands for full alignment with the stable Leslie angle and white stands for non-alignment.

$R = 10^6$, $\beta = 1.2$. At lower temperatures, the DL and the DG mode persist for a larger range of De. Near the nematic-isotropic transition, only the planar mode exists, while the defect modes (DG) and (DL) disappears. The simulations show that control of texture formation is feasible by temperature and shear rate selection. To obtain a texture free sample, a sufficiently high shear rate (De) and temperature (U) are necessary.

5. Conclusions

This work presents simulations of structure formation for capillary and simple shear flow of two important liquid crystalline materials, taking into account the couplings between velocity and molecular orientation. The results of these simulations capture the formation of characteristic macro and micro-textural phenomena and provide new knowledge on the role of viscous and elastic effects in the processing flow of these materials, used as a precursor in the production of advanced fibers.

For pressure-driven capillary flows of carbonaceous mesophases, the average molecular orientation model shows that degeneracy and nonlinearity drive the emergence of banded patterns, which are a characteristic feature in NLCs; for instance, in the carbon fibers melt spun from mesophase precursors. In addition, the solution multiplicity and nonlinearity provides a second

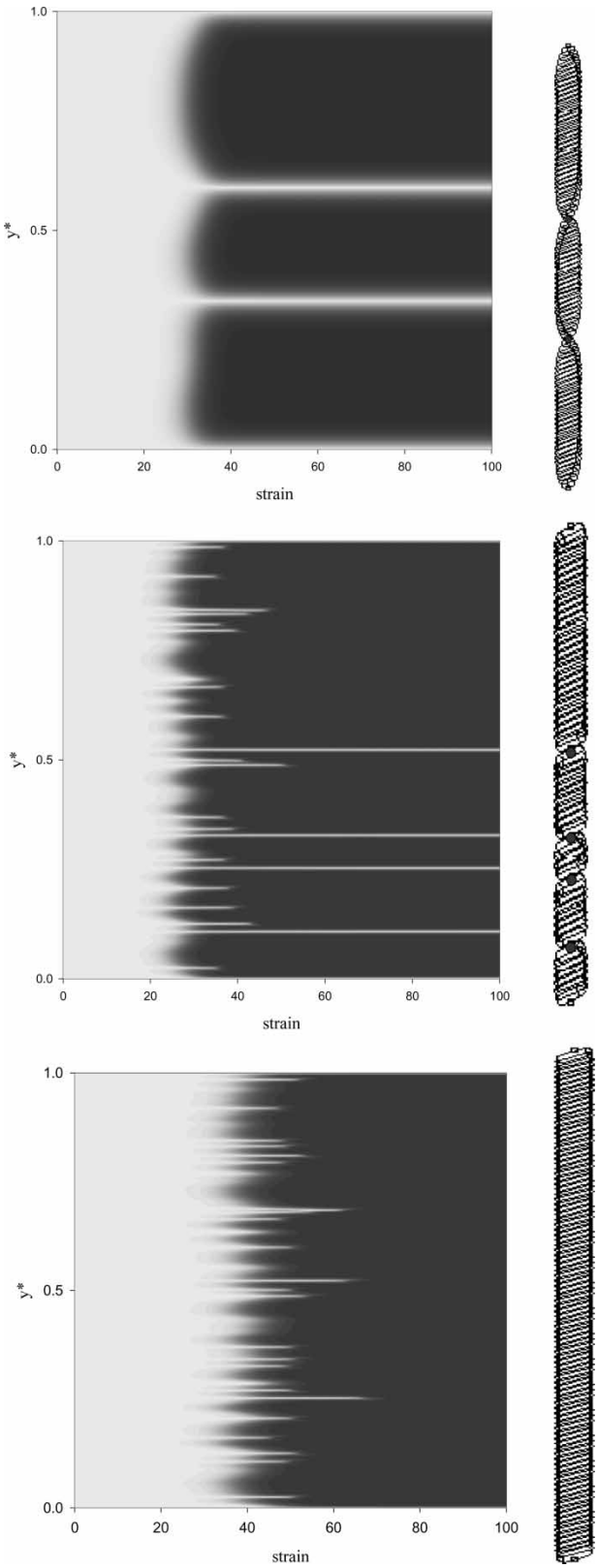

Figure 7. Computed gray scale visualization of director component n_z ($0 \leq y^* \leq 1$) as a function of strain, for nematic LCPs under simple shear. Black represents in plane orientation ($n_z = 0$) and light orientation along the vorticity ($n_z = 1$): (a) DL mode, De $= 0.05$, $U = 4.5$, $R = 10^6$; (b) DG mode, De $= 2.4$, $U = 4.25$, $R = 10^6$; (c) P mode, De $= 4.6$, $U = 4.5$, $R = 10^6$. In the right, there are the corresponding representative computed visualizations of the steady state solutions obtained for high values of strain. The dark dots represent the inversion twist walls.

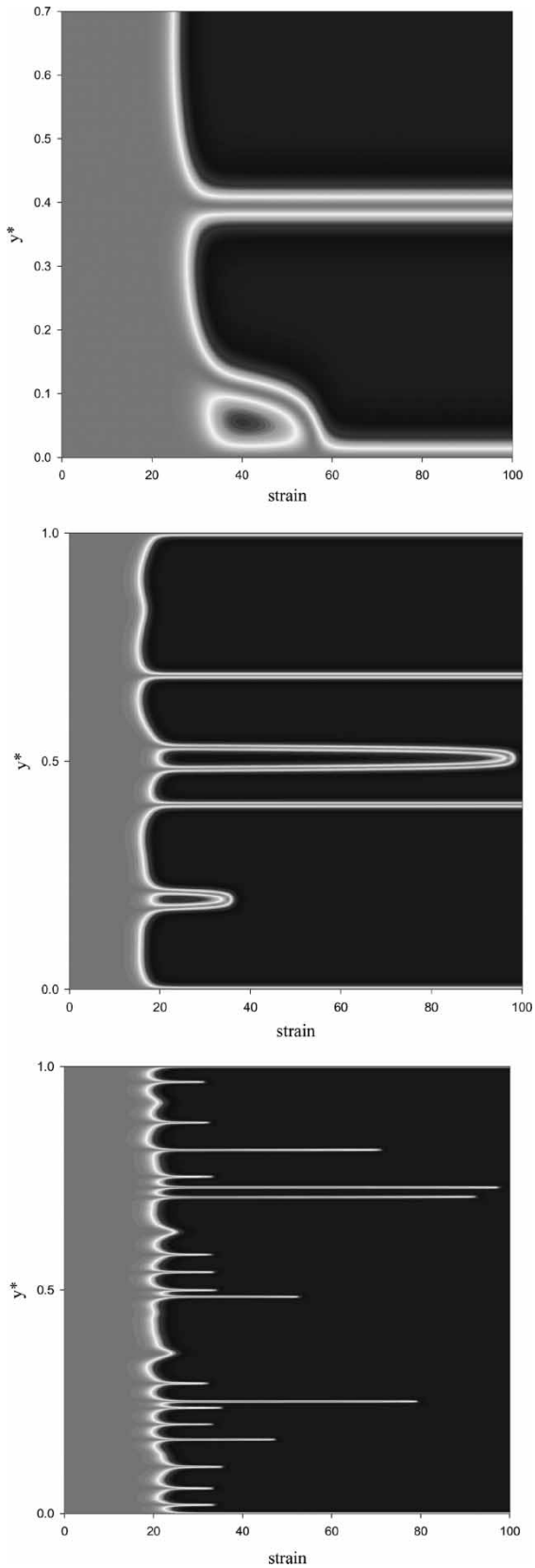

Figure 8. Computed visualization of director component n_z ($0 \leq y^* \leq 1$) as a function of strain, for nematic LCPs under simple shear. Black represents in plane orientation ($n_z = 0$) and light orientation along the vorticity ($n_z = 1$): (a) wall–bounding surface interaction in the DL mode, De $= 0.01$, $U = 4$, $R = 10^6$; (b) wall–wall interaction in DL mode, De $= 0.04$, $U = 3$, $R = 10^5$; (c) wall pinching in P mode, De $= 0.83$, $U = 3.5$, $R = 10^6$.

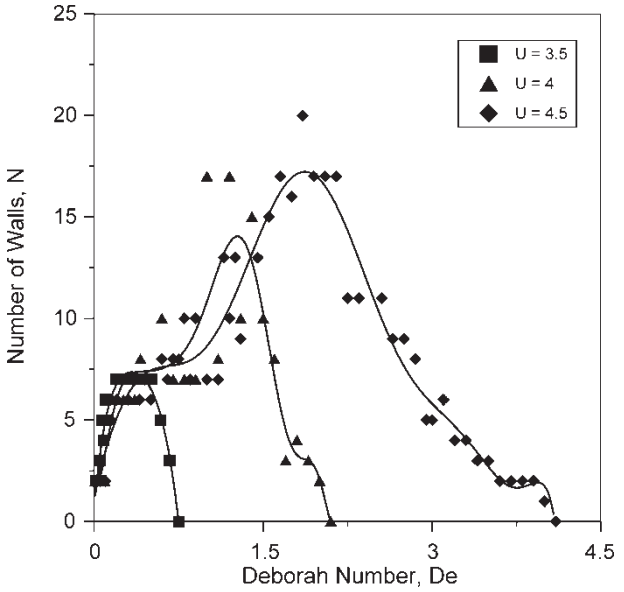

Figure 9. Number of inversion walls (N) as a function of De number, for different nematic potentials (U), for nematic LCPs under simple shear.

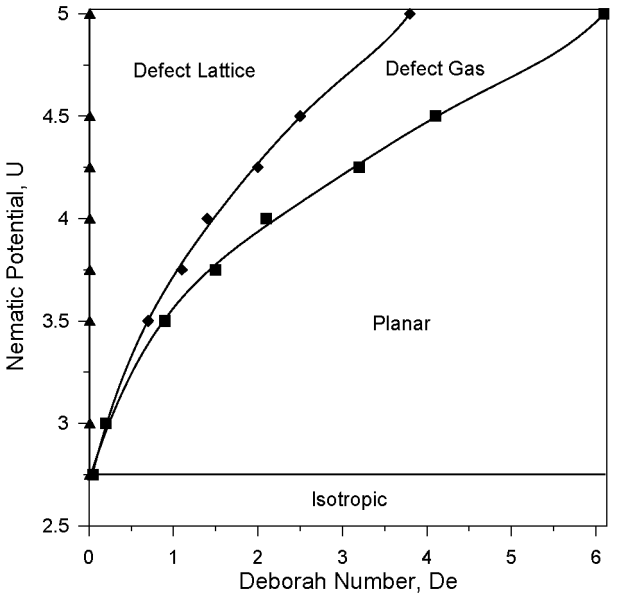

Figure 10. Rheological phase diagram of flow-aligning thermotropic liquid crystal polymers on the temperature (U)–shear rate (De) plane for $R = 10^6$, $\beta = 1.2$.

hydrodynamic mechanism to drive the emergence of structure with intermediate length scales.

For simple shear flow, the classical theories of nematodynamics applied to thermotropic rod-like flow aligning nematic polymers predict that, as the shear-rate increases, the pathway between an oriented non-planar state and an oriented planar state is through texture formation and coarsening. The two shear-rate-dependent dimensionless numbers that control the texture formation and coarsening process are the Er and De numbers. The emergence of texture is independent of De number, and occurs at $\mathrm{Er} = 10^4$. As the shear rate increases and $\mathrm{Er} > 10^4$ the first texture that arises is a lattice of inversion walls. Further, increases of the shear rate, ignite the coarsening processes, and replace the DL with a DG. Finally, at higher shear rates, a monodomain state emerges, and the texture vanishes since coarsening overpowers defect nucleation. It is found that the texture evolves (from unoriented monodomain, DL, DG, to oriented monodomain) is remarkably consistent with the textural transition of sheared lyotropic tumbling nematic polymers. Thus the presented simulation of hydrodynamic meso-scale texture formation is able to provide fundamental principles for control and optimization of structures in liquid crystal materials. Temperature and shear rate are efficient fields to control the grain size of the texture. High temperatures and shear rates lead to defect free monodomains. The flow simulations are shown to be in full agreement with experimental observations.

Acknowledgements

This work was supported primarily by the ERC Program of the National Science Foundation under Award Number EEC-9731680. DG and LRPdAL also gratefully acknowledge the support of Natural Sciences and Engineering Research Council of Canada, and the Eugenie Ulmer Lamothe Fund of the Department of Chemical Engineering at McGill University.

References

[1] A.D. Rey, M.M. Denn. Dynamical phenomena in liquid-crystalline materials. *Ann. Rev. Fluid Mech.*, **34**, 233–266 (2002).
[2] R.G. Larson. *The Structure and Rheology of Complex Fluids*, Oxford University Press, New York (1999).
[3] G. Goldbeck-Wood, P. Coulter, J.R. Hobdell, M.S. Lavine, K. Yonetake, A.H. Windle. Modelling of liquid crystal polymers at different length scales. *Mol. Simul.*, **21**, 143–160 (1989).
[4] P.G. de Gennes, J. Prost. *The Physics of Liquid Crystals*, Oxford University Press (1993).
[5] F.R.S. Chandrasekhar. *Liquid Crystals*. University Press (1992).
[6] F. Beekman, A.D. Gotsis, B. Norder. Transient and steady-state rheological behavior of the thermotropic liquid crystalline polymer Vectra B950. *J. Rheol.*, **40**(5), 947–966 (1996).
[7] V.M. Ugaz, W.R. Burghardt, W. Zhou, J. Kornfield. Transient molecular orientation and rheology in flow aligning thermotropic liquid crystalline polymer. *J. Rheol.*, **45**, 1029–1063 (2001).
[8] A. Sonnet, A. Kilian, S. Hess. Alignment tensor versus director: description of defects in nematic liquid crystals. *Phys. Rev. E*, **52**, 718–722 (1995).
[9] P.T. Mather, D.S. Pearson, R.G. Larson. Flow patterns and disclination-density measurements in sheared nematic liquid crystals I: flow-aligning 5CB. *Liq. Cryst.*, **20**(5), 527–538 (1996).
[10] P.T. Mather, D.S. Pearson, R.G. Larson. Flow patterns and disclination-density measurements in sheared nematic liquid crystals II: tumbling 8CB. *Liq. Cryst.*, **20**(5), 539–546 (1996).
[11] D.J. Graziano, M.R. Mackley. Disclinations observed during the shear of MBBA. *Mol. Cryst. Liq. Cryst.*, **106**, 103–119 (1984).
[12] A.P. Singh, A.D. Rey. Effect of long range elasticity and boundary conditions on microstructural response of sheared discotic mesophases. *J. Non-Newtonian Fluid Mech.*, **94**, 87–111 (2000).

[13] L.R.P. de Andrade Lima, A.D. Rey. Poiseuille flow of Leslie–Ericksen discotic liquid crystals: solution multiplicity, multistability, and non-Newtonian rheology. *J. Non-Newtonian Fluid Mech.*, **110**(2–3), 101–147 (2003).
[14] L.R.P. de Andrade Lima, A.D. Rey. Computational modeling of ring textures in mesophase carbon fibers. *Mat. Res.*, **6**(2), 285–293 (2003).
[15] L.R.P. de Andrade Lima, A.D. Rey. Linear and nonlinear viscoelasticity of discotic nematics under transient Poiseuille flows. *J. Rheol.*, **47**(5), 1261–1282 (2003).
[16] T. Tsuji, A.D. Rey. Effect of long-range order on sheared liquid crystalline materials. Part I: Compatibility between tumbling behavior and fixed anchoring. *J. Non-Newtonian Fluid Mech.*, **73**, 127–152 (1997).
[17] S.K. Ho, A.D. Rey. Orienting properties of discotic nematic liquid crystals in Jeffrey–Hamel flows. *Rheol. Acta.*, **30**, 77–88 (1991).
[18] L. Wang, A.D. Rey. Pattern formation and non-linear phenomena in stretched discotic nematic liquid crystal fibers. *Liq. Cryst.*, **23**, 93–111 (1997).
[19] D. Grecov, A.D. Rey. Shear-induced textural transitions in flow-aligning liquid crystal polymers. *Phys. Rev. E*, **68** (2003) 061704–1–20.
[20] R.G. Larson, D.W. Mead. The Ericksen number and Deborah number cascades in sheared polymeric nematics. *Liq. Cryst.*, **15**(2), 151–197 (1993).
[21] W.H. Han, A.D. Rey. Shear flow-induced Chiral–Achiral transition and twisted textures in a nematic polymer. *Phys. Rev. E*, **49**(1), 597–614 (1994).